RESEARCH ARTICLE

ADVANCED
PHOTONICS
RESEARCH
Open Access

www.adpr-journal.com

Collectively Enhanced Giant Circular Dichroism of Germanium Nanohelix Square Lattice Arrays

Günter Ellrott, Paul Beck, Vitaliy Sultanov, Sergej Rothau, Norbert Lindlein, Maria Chekhova, and Vojislav Krstić*

Circular dichroism is a unique chiroptical signature of the chirality of a system and is a prevalent way to characterize and distinguish systems on a fundamental level and for their technological applicability. Thus, engineering and maximizing the chiroptical response of a single chiral object or a metasurface composed of chiral entities is a formidable task. Current efforts strongly focus on individual metallic nanostructures and their periodic ensembles to harvest on (resonant) plasmonic properties and interactions. This route, however, waives the advantages of high-refractive-index nanoscale materials embracing low dissipative losses at optical wavelengths and electromagnetic fields penetrating and propagating in such materials. Herein, a strong circular dichroism is demonstrated in square lattices of nanohelices made of the high-refractive-index semiconductor germanium, with dissymmetry factors outperforming metal-based ensembles. The observation of a much higher dissymmetry emerges for illumination with spatially coherent light, in comparison to spatially incoherent light. High dissymmetry is attributed to cooperative coupling between single helices, resulting from the combination of dielectric resonances of both the individual helical building blocks and the highly ordered lattice.

1. Introduction

The interaction between chiral systems and light ignites continuous interest and is actively investigated.[1–4] Composite materials consisting of chiral constituents are of particular interest as a platform to study light–matter interaction. Chiral metasurfaces are one type of such materials exhibiting circular dichroism (CD), which makes them, for instance, usable as thin circular polarizers[5–11] and in related applications such as metalenses[12,13] and metaholography.[14] Specifically, in comparison to solely 2D structured metasurfaces, 3D chiral metasurfaces are highly intriguing. Such types of systems are made of periodically ordered individual chiral entities with subwavelength spacings and can be envisioned to have enhanced optical performance and/ or novel (quantum) functionalities[15–18] compared to their 2D counterparts.

Currently, glancing angle deposition (GLAD) approaches are frequently used to manufacture 3D chiral metasurfaces[19–21] with a focus on plasmonic materials, such as, for example, gold,[22] silver,[23,24] or nickel.[19,25] That is, the optical properties of these systems are mainly determined by chiroplasmonic mechanisms and responses of the individual entities, which can be resonantly excited upon illumination with circularly polarized light.[26]

However, using optical resonators made from high-refractive-index semiconductors like germanium or dielectrics as building blocks for 3D chiral metasurfaces can provide significant advantages compared to their plasmonic counterparts. This includes low dissipative losses at optical wavelengths,[27] the circumstance that the electromagnetic field can penetrate into and propagate within the material and the chiral structure allowing for simultaneous excitation of (localized) electric and magnetic di- and multipole modes.[28] Therefore, near-field enhancement of both electric and magnetic fields is expected in the volume of the material in addition to any surface-related contributions. While there have been reports on structures made from insulators such as SiO$_2$[20] or semiconductors[29–32] by GLAD, the cooperative CD response was not addressed albeit this can be expected to boost the metasurfaces' performance. Germanium as a material for oblique vapor deposition has been investigated as a method for columnar growth,[31,33] however, not to achieve helical structures.

In this work, we report on the CD at visible wavelengths of germanium nanohelix square lattice arrays on transparent sapphire substrates grown by GLAD and disclose the underlying cooperative character of the chiroptical response by separately measuring CD for both spatially coherent and incoherent light. The physical separation (void) between two neighboring nanohelices in an array is about an order of magnitude smaller than for all wavelengths used (subwavelength range) and the feature sizes

G. Ellrott, P. Beck, V. Sultanov, S. Rothau, N. Lindlein, M. Chekhova, V. Krstić
Department of Physics
Friedrich-Alexander-Universität Erlangen-Nürnberg (FAU)
Staudtstr. 7, 91058 Erlangen, Germany
E-mail: vojislav.krstic@fau.de

P. Beck, V. Sultanov, M. Chekhova
Max Planck Institute for the Science of Light
Staudtstr. 2, 91058 Erlangen, Germany

of the helical structures are in the ≈100 nm range. It is noteworthy that at these helical feature sizes one reaches already into the quantum realm considering the excitonic Bohr radius in Ge, which is generally taken as 24.3 nm.[34–38]

Different lattice periods and helical pitches were used to investigate their influence on the CD when using spatially coherent and incoherent light illumination. The use of such two light sources allows for tracing the coupling between the individual helices as in the incoherent case the small coherence area limits the number of helices for collective interaction, while using a spatially coherent light source allows strong coupling among many of them. That is, the respective cooperative behavior can be unveiled by qualitative and quantitative differences in the CD wavelength dependence using the two types of measurements. We demonstrate that the dissymmetry factor employed to quantify the CD boosts in the spatially coherent case and also exceeds that of most other known 3D chiral metasurfaces even for incoherent light. Furthermore, we corroborate our experimental findings by electrodynamic finite-difference time domain (FDTD) simulations. These findings represent the first steps in the direction of high-performance 3D dielectric chiroptical platforms.

2. Results

2.1. Germanium Nanohelix Square Lattice Arrays

The manufacturing of 3D chiral metasurfaces is often hindered by a lack of control to produce highly ordered, scalable 3D structures. Standard manufacturing techniques, such as UV or electron beam lithography, only allow good control of 2D. Other techniques, such as direct electron beam-induced deposition[39] or stacking of individual achiral structures,[9,40,41] have a very limited throughput which makes them unsuitable for manufacturing large areas. GLAD enables fast manufacturing of spatially extended metamaterials while maintaining control over 3D.[42] In this technique, the shadowing effect enables controlled deposition of various structures. It has been shown that unseeded self-shadowing leads to (continuous) helical films with randomly arranged and often collapsed structures, while highly uniform individual structures arranged in a well-defined periodic way can be grown exclusively when using a suitable seed prepatterning of the substrate.[20] Typically, high–melting-point materials require active substrate cooling during growth. Here we use a more advantageous approach based on local passive thermal shielding,[19] enabling the production of well-defined chiral structures with sub-100 nm feature sizes. Moreover, this approach is in principle integrable into existing manufacturing processes due to its passive nature. A schematic of the growth of helical nanostructures using GLAD and a top-down view on an array is shown in **Figure 1** (top row; see Experimental Section). The middle and bottom rows of Figure 1 display scanning electron microscopy (SEM) images of individual germanium helices grown in arrays of different lattice spacing (lateral distance between the helices) l_S on sapphire and mechanically removed for imaging. Two different sets of samples have been grown, with helical pitches of 180 and 360 nm, respectively, and two full turns each. The seed height and diameter were kept constant for all samples (see Experimental Section). The quality of the helix

arrays indicates that sapphire is a suitable substrate for the employed passively cooled GLAD process.[19]

The middle row in Figure 1 displays right-handed (D) helices with a pitch of 180 nm. From left to right, l_S increases from 150 to 450 nm. The helix wire diameter increases for larger l_S, despite the same seed dimensions. Eventually, the helical shape disappears at $l_S = 450$ nm, and the structure consists of vertical columns instead of helices. The bottom row in Figure 1 shows the SEM images of D-helices with 360 nm pitch. At an l_S of 150 nm, the individual helices of the array appeared rather thin and coarse and by large collapsed. Instead, at 300 nm spacing, the 360 nm pitch helices appear to be best defined. At the largest l_S of 450 nm, a thickening of the wire a helix consists of can be observed again as in the case of 180 nm pitch helices with 450 nm lattice spacing. The changes observed with the lattice spacing can be explained by the reduction of the effectiveness of shadowing between seeds during growth at with larger l_S. That is, for each individual seed, the shadowing by nearest-neighbor and next-nearest-neighbor seeds is reduced with growing l_S leading to more material being deposited locally at each helix growth site.

2.2. Circular Dichroism: Transmission Dissymmetry Factor

To disclose single-helix and collective contributions to the overall observed response, we perform two separate CD measurements. First, we employ a spatially incoherent thermal white light source (see Experimental Section) to gather the chiroptical response of a single nanohelix or a small group of them. Second, on the same sample, we use a spatially coherent supercontinuum white light source to obtain the full cooperative chiroptical response. In both setups, a linear polarizer (LP) and a rotatable quarter waveplate (QWP) are used to prepare the incident left- and right-circularly polarized light. As a measure for CD, we use a transmission dissymmetry factor g, defined as

$$g = \frac{2(T_L - T_R)}{T_L + T_R} \tag{1}$$

with T_L and T_R denoting the transmitted intensity of left and right circularly polarized incident light, respectively.[43,44] The maximum modulus of g is 2. The normalisation factor $T_L + T_R$ accounts for the total transmission. This definition is similar to the so-called Kuhn's factor, which is based on absorbance instead of transmission, requiring the simultaneous measurement of transmission and reflection combined with normalization to the incoming light power.[32]

2.3. Circular Dichroism Response with Spatially Incoherent Thermal Light Source

The experimental scheme for the measurements with the spatially incoherent light source is shown in **Figure 2**a. The light passes through a monochromator to continuously vary the wavelength from 550 to 750 nm. After transmission through the samples, the light is captured by a camera with the pixel values in the image proportional to the transmitted intensity. Figure 2b shows an exemplary measurement of the transmission dissymmetry factor g for D- and L-helices with a pitch of 360 nm and
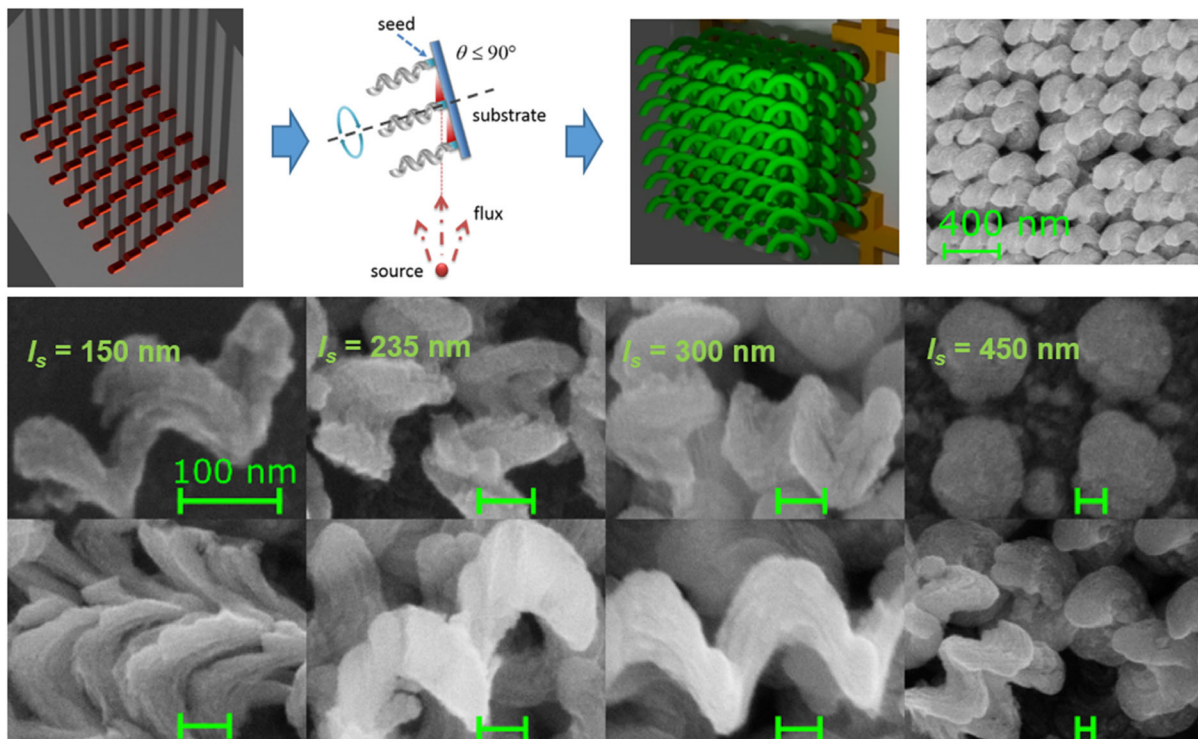
Figure 1. Schematic GLAD process and Ge helices grown on sapphire. Top row: Principle of nanohelix array growth by GLAD. The rightmost panel shows an exemplary SEM image of an array of D-helices with a pitch of 360 nm and a lattice spacing l_S of 300 nm. The original rectangular pattern of the seeds is clearly visible after growth. The nanohelices are well defined and closely packed, and, importantly, individually free standing. Middle row: Ge nanohelices with 180 nm helix pitch and two turns. l_S increases from left to right as 150, 235, 300, and 450 nm. The major diameter is 100, the wire thickness is 60 nm for helices with the lowest spacing and increases up to 90 nm for large spacings (all helix dimensions are subject to 10–15% experimental variation). Bottom row: Ge nanohelices with 360 nm helix pitch and two turns. l_S increases the same way as for the middle row. All scale bars are 100 nm. The major diameter is 190 nm. The wire thickness increases with spacing from 60 to 90 nm (all dimensions are subject to 10–15% experimental variation).

$l_S = 300$ nm (all other data summarized in Supporting Information). The standard deviation is obtained (light gray) from the camera image of four individual fields each consisting of ≈2500 pixels. As expected, helices of opposite handedness show dissymmetry factors of the same magnitude and inverse signs. Over the observed wavelength range, a maximum can be seen at 710 ± 5 nm, with a slow increase from 550 to 700 nm and a steep decline toward 750 nm.

In Figure 2c, we compare the measurement shown in Figure 2b to classical electromagnetic FDTD simulations, where we consider on the one hand the case of an infinitely extended array of nanohelices and on the other hand a single helix. The maximum value of the dissymmetry factor is much larger for the infinite array than for the single helix. This can be attributed to an enhanced chiroptical response due to coupling among the helices in the highly ordered lattice and collective resonances emerging in the infinite array. Further, the maximum value of g can be found at different wavelengths for the two cases, which in the case of the single helix leads to a maximum lying outside the experimental wavelength range. The curve corresponding to the experimental data is located between the two extreme cases considered in the simulation though closer to the single-helix case. This is expected as collective effects are caused by the interaction of a small number of helices. However, this number is limited by the coherence area of the used light source. In the

following, the full cooperative behavior of the helix arrays is examined using a supercontinuum light source.

2.4. Circular Dichroism Response with Spatially Coherent Supercontinuum Light Source

The measurement approach with the supercontinuum source (**Figure 3**a; see Experimental Section) is similar to the one for the thermal light source described earlier. After preparation of the circular polarization state, a spatially coherent beam of light from the supercontinuum source is focused onto the sample. The resulting focal spot has a diameter of around 100 μm. Here, we note that in combination with the supercontinuum peak pulse power of 50 mW employed in the experiment, the maximum field strength in the focal plane is limited to about 5×10^4 V m^{-1}. Therefore, we can neglect the contribution of any nonlinear effects to the optical response of the nanohelix arrays.

The transmitted light is captured by imaging the sample plane onto a CCD camera. The wavelength is varied from 520 to 800 nm, while taking a CCD image at each step to record the spectral transmission of left- and right-handed circularly polarized light (Figure 3b). The total transmission is obtained by integrating over the red dotted square, corresponding to an
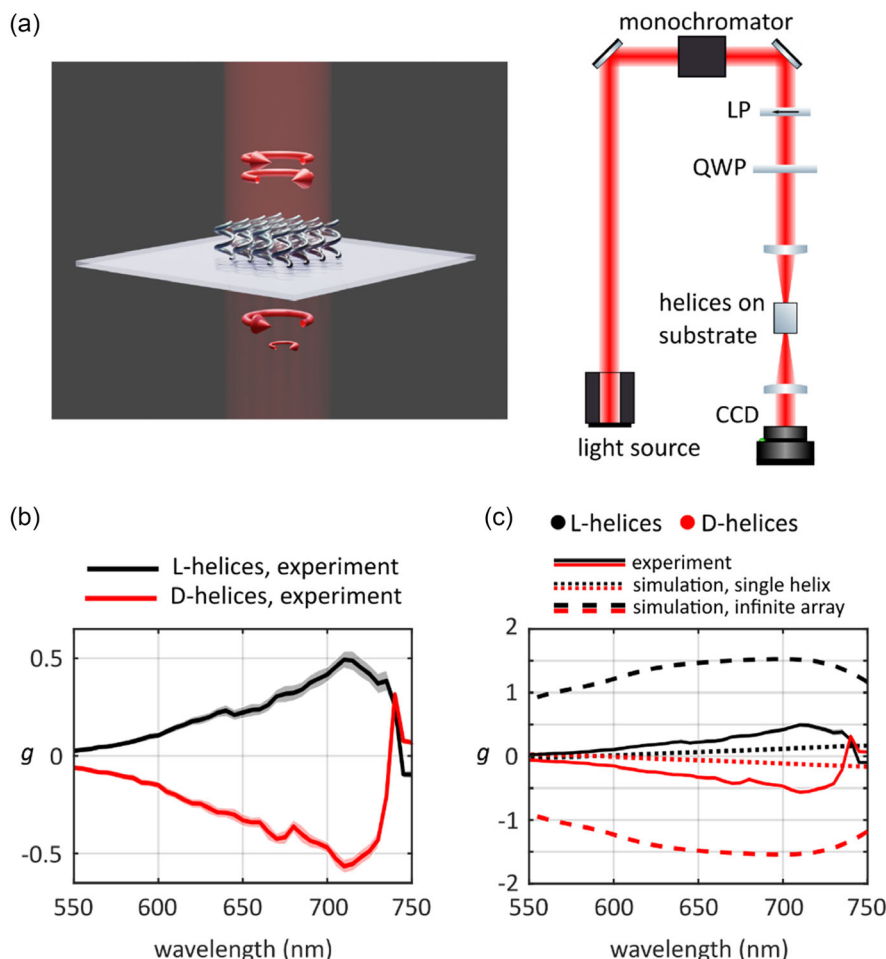
Figure 2. Measurement of transmission dissymmetry factor as a function of wavelength with spatially incoherent thermal light. a) Left: Illustration of the circular dichroitic action of a nanohelix array. The arrows indicated the polarization of the incoming (top) and transmitted (bottom) light. Right: Schematic of the setup. Specific wavelengths are selected by a monochromator using white light from a thermal source. The selected light/wavelength is then circularly polarized using a horizontal LP and a QWP. b) g for an L- and D-helix array with 2 turns of 360 nm pitch and an l_S of 300 nm. The major diameter of each helix is ≈190 nm. The wire thickness is ≈60 nm. Opposite handedness of the helices leads, as expected, to inverted signals. Shadow regions denote the standard deviation of the signals collected from four different fields. c) Comparison of the same measurement as in b to classical electrodynamics simulations considering a single helix and an infinite array, respectively. Neither simulation fits the observed results, indicating a local collective effect being present but limited by the spatial incoherence of the light source.

area of $42 \times 42\,\mu m^2$. We chose this size because in the edge region of the $100 \times 100\,\mu m^2$ field helices are imperfect, although incomplete helices are only present within 15 μm from the edge. The $42 \times 42\,\mu m^2$ window is taking twice this edge region into account. The approximation of an infinitely extending array is still justified at a 42 μm size, as the lattice spacings are two to three orders of magnitude smaller. Arrays with different l_S and helical pitches of 180 and 360 nm (Figure 3c,d, respectively) were studied. To prove the reproducibility of both the measurement and the fabrication procedure, we perform measurements on multiple arrays of the same l_S and pitch and both handednesses. In order to simplify the comparison in terms of CD dissymmetry, we take the average value of the transmission dissymmetry factor of several structurally equivalent L- and D-samples. For this average $\bar{g}$, the statistical standard deviation is then determined and indicated as a gray shadowed region around the black curves in Figure 3.

The data in Figure 3 clearly demonstrate that the spectral shape and the maximum of the dissymmetry factor strongly depend on both l_S and helix pitch. That is, it is possible to tune the array response via the variation of these parameters. We also find $\bar{g}$ values of up to 1.4, which is remarkably high considering that 2 is the absolute physical maximum for the dissymmetry factor (cf. Equation (1)). In particular, the measurements reveal an exceptionally strong and broadband chiroptical response of the majority of the nanohelix arrays.

Figure 3c,d also shows the results of the classical electrodynamic FDTD simulations (orange curves), in which we consider an infinitely extended periodic array of helices illuminated by a circularly polarized plane wave. The first approximation is valid because the arrays are much larger than the wavelength of the light and the illuminated area spans several hundred unit cells. The planewave approximation can be justified by the fact that the beam is weakly focused to a spot slightly larger than the size of
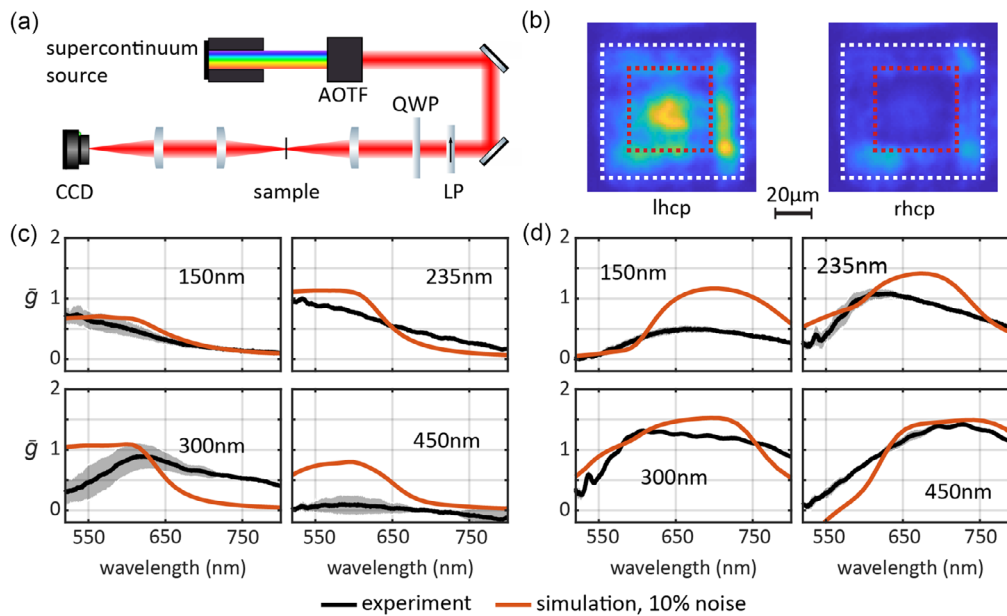
2300159 (4 of 8)

**ADVANCED
SCIENCE NEWS**

www.advancedsciencenews.com

**ADVANCED
PHOTONICS
RESEARCH**
Open Access

www.adpr-journal.com

Figure 3. Measurements of the transmission dissymmetry factor as a function of wavelength with a spatially coherent supercontinuum source. a) Experimental setup for the supercontinuum source. White light originating from the source is passed through an AOFT, then a LP, and a QWP prior to illuminating the sample. The transmitted light is collected with a charge-coupled device (CCD) camera. b) Exemplary CCD images for an L-helices array with a pitch of 360 nm and $l_S = 450$ nm, recorded at a wavelength of 730 nm (l/rhcp = left-/right-handed circular polarized light). The area of the full array is indicated by the white rectangle, while the red square corresponds to the region considered to obtain the transmitted intensity. To limit unwanted influence from edge effects, the observed area was limited to a 42 by 42 μm^2 region (red square). c,d) Comparison of measured (black curves) and FDTD simulation (orange curves) data of $\bar{g}$ for arrays with (c) 180 nm and (d) 360 nm helical pitch at different l_S. We perform measurements on multiple arrays of the same l_S and pitch and both handednesses to calculate $\bar{g}$ of two arrays of L- and D-helices (gray shadowing corresponds to the standard deviation). The orange curves correspond to FDTD simulations including a relative noise of 10%.

the arrays using a lens with a focal length of 100 mm. We also accounted for the noise in the experimental data (cf. Supporting Information). This noise originates from the camera noise and from scattering and diffraction of light by the edges of the helix arrays. The latter results in polarization-independent transmission. To account for this, we consider a noise level of 10% relative to the maximum transmission (orange curves). As the actual noise level can strongly vary from sample to sample, we took the value of 10% as a rough conservative estimate for all arrays. As expected, this leads to a decrease of g in the short-wavelength range, where the transmission of germanium is significantly reduced due to a strong absorption at wavelengths below $\approx$600 nm. The results of the simulations including noise are in part in reasonable agreement with the experimental data. The deviations between the purely electrodynamic simulation and experiment can thus on one hand be attributed to potential influence of quantum-related interactions on the subwavelength scale and energetic quantization of charges in the nanohelices.[45,46] Also, the surface roughness of the fabricated helices is not accounted for in the simulation. The actual dimensions and thus also the spacing of the helices are not perfectly uniform across the entire array, as shown in Figure 1. Finally, the experiment differs from the simulation regarding the spatial extent of the array. The number of array periods considered in the experiment is on the order of 100, while in the simulation, the array is perfectly infinite. Despite this being a very good approximation to the real-world situation, the finiteness of the array in the

experiment certainly influences the spectral distribution of the dissymmetry. That is, despite being a good approximation to the situation in the experiment, the FDTD simulations do not encompass all aspects of the latter. Nevertheless, modeling allows to gain insight into qualitative expectations in the difference of chiroptical response when using spatially coherent and incoherent light illumination and enables to spot in the experimental results deviations from a purely electrodynamic picture. Further details regarding the numerical methods can be found in the Supporting Information.

3. Discussion

We observe chiroptical activity from both spatially coherent and incoherent illumination of the helix arrays. However, the dissymmetry factor obtained for illumination with spatially coherent light is markedly larger. In particular, a giant dissymmetry factor of up to 1.4 ± 0.05 can be achieved in the case of spatially coherent illumination. This is a witness of an enhanced cooperative response, that is, increased coordinated coupling between the resonances of the individual helices. The results obtained with the supercontinuum source match the FDTD simulations for infinite arrays better than the ones obtained with the thermal light source. This further strengthens the conclusion that spatially coherent illumination that leads to an enhanced collective coupling between the individual helices.

To put the observed magnitudes from this work into perspective, a comparison to different 3D structures exhibiting CD reported in literature is summarized in **Figure 4**.[8,9,22,44,47] To allow for comparison between different works, we introduce here the dissymmetry factor g_{1000} serving as a figure of merit (cf. Supporting Information). In essence, it is the transmission dissymmetry factor at a hypothetical material thickness of 1000 nm, deduced on the basis of the reported experimental data a structure with its specific dimensions shows and accounting for the physical nonlinearity and modulus limit of 2 of the transmission dissymmetry factor as per Equation (1).

The g_{1000} values in Figure 4 demonstrate that our arrays surpass the performance of GaAs-based chiral semiconductor metastructures.[9] Remarkably, already under incoherent light, the dissymmetry factor of Ge nanohelix arrays is clearly larger compared to plasmonic metamaterials. Under spatially coherent light, they outperform them with values close to $g_{1000} = 2$.[8,22,43,44] This is extraordinary considering the absence of plasmonic field enhancement in the employed Ge structures which are governed by volume dipoles and multipoles. It should be noted that Ge can be considered as a high-refractive-index dielectric governing the resonant behavior of the individual helices. This is in stark contrast to metallic nanostructures, for which the resonances and the resulting electromagnetic field enhancements are of plasmonic nature.[23] The observed broadband enhancement of CD is thus attributed to a combination of resonant excitation of the individual helices and an increased cooperative response due to the highly ordered subwavelength arrangement. Specifically, the latter could be shown to be strongly influenced by the choice of l_S and helical structural parameters.

All these points show that our Ge nanohelix arrays represent a periodic assembly of dielectric chiral resonators. The periodic arrangement of the helices enables coordinated coupling among them upon illumination with spatially coherent light. The emerging collective resonances strongly enhance and modify the chiroptical response of the array. It might also be considered that each individual helix within the lattice acts similar to a quantum-dot-like entity embedded in a resonant structure formed collectively by the crystal constituents[48] (surrounding helices).

4. Conclusion

We have demonstrated that Ge nanohelix square lattices, consisting of physically subwavelength packed, highly ordered, and free-standing individual nanohelices with different helical pitches and lattice spacing, show a strong chiroptical response, which we quantified by the transmission dissymmetry factor. We found values of dissymmetry of up to 1.4 which compete with other comparable metastructures. The wavelength at which the maximum dissymmetry can be found depends on both helix pitch and lattice spacing. Noteworthy, the dissymmetry factor is high across a wide wavelength range. This characteristic makes our Ge nanohelix arrays an extremely promising candidate for a nonplasmonic 3D metamaterial technology platform.[5–14] The dissymmetry factor is much higher for illumination with spatially coherent light from a supercontinuum source, compared to spatially incoherent illumination. Therefore, the strength of the CD response in our samples is predominantly attributed to the cooperative enhancement of chiral dielectric resonances. The arrays investigated can be considered as periodic assemblies of chiral nanocavities, with an intracavity electromagnetic field distribution depending on the handedness of light and helix. The restricted resonator volume leads to both strong confinement and enhancement of the electromagnetic fields, augmenting the strength of light–matter interactions. Besides that, the comparison of the classical FDTD calculations with the experimental data suggests the presence of additional quantum-related effects including the subwavelength range.

5. Experimental Section

Nanohelix Array Design and Growth: Sapphire substrates were prepared for GLAD with a square lattice pattern of seeds. Seed patterning was done using standard electron beam lithography and subsequent evaporation of Ge. The seed height was 30 nm and the diameter 60 nm for all samples produced. Sapphire offered good thermal conductivity (several tens of $\mathrm{W\,mK^{-1}}$), optical transparency at visible wavelengths, and no optical activity. Thus, this substrate is an ideal choice for growing nanohelix arrays without active substrate cooling and the subsequent use of such samples for optical studies. The seed pattern design determined the spacing between individual helices within the helix array after growth. As lattice constants, we used 150, 235, 300, and 450 nm. During the GLAD process, a passive heat shield technique[19] using standard UV resist was used to protect the regions without seed patterning. The substrate was mounted with its normal being at an angle of 88° to the incoming material in the evaporation chamber on a rotatable mount with the rotation of the driving motor adjusted in a feedback loop to the real time measured deposition rate. The rotational speeds were varied such that helix arrays with two different helical pitches of 180 and 360 nm were grown.

Thermal Light Source Measurements: White light from a spatially incoherent thermal source was sent through a monochromator to select specific wavelengths. Radiation at a selected wavelength was then circularly polarized using a horizontal polarizer and a QWP. The orientation of the QWP was controlled by a measurement logic to automatically take
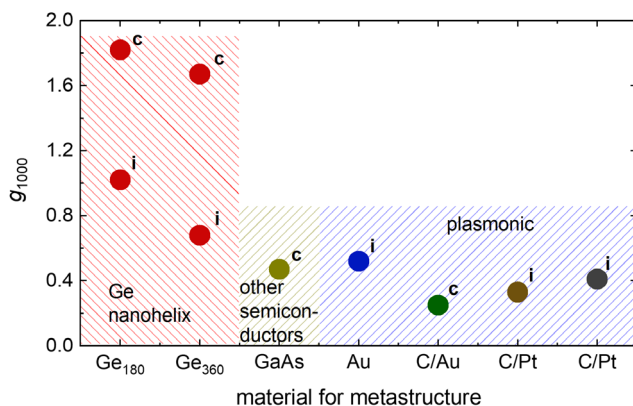

Figure 4. Comparison of maximum unit-length normalized transmission dissymmetry factors to similar 3D metastructures made of different materials. Points noted with *c* are results obtained using coherent incident light,[9,47] *i* denotes incoherent light.[8,22,44] The red area are results presented here with 2 turns of 180 and 360 nm pitch (indicated by index). The green area shows results obtained from other semiconductors, with the highest resulted value corresponding to $g_{1000} = 0.75$. The blue area is a summary of results obtained from plasmonic materials. The g_{1000} was in the range of 0.1–0.5, whereas our germanium arrays display a much larger effect even with incoherent light.

images using a digital camera behind the device under test with both left and right circular polarizations. The response of each pixel of the camera could be individually detected. The layout of the setup is pictured in Figure 1. Each pixel of the obtained images evaluated the dissymmetry factor g independently and a histogram of all values gave a Gaussian distribution with the mean value and an error determined from the distribution's standard deviation. The gray-and red-shadowed areas around the curves in Figure 2b corresponded to the resulting standard deviation of these measurements.

Supercontinuum Light Source Measurements: To generate light with a large coherence area and tunable wavelength, we used a commercial supercontinuum source (KOHERAS SuperK Extreme, EXU-6). The supercontinuum was generated by feeding a 1065 nm seed laser pulse into a nonlinear photonic crystal fiber, using a repetition rate of 78 MHz and a seed pulse length of 5 ps. The average power of the resulting supercontinuum light was around 10 μW, resulting in a peak power of around 50 mW. Weakly focusing the beam to a spot size of around 100 μm × 100 μm resulted in a maximum electric field strength of $\approx 5 \times 10^4 \, V \, m^{-1}$. An acousto-optic tunable filter (AOFT) was used to select the wavelength of the light. The resulting monochromatic beam, having a diameter of approximately 1.5 mm, was passed through a LP and a QWP to generate the desired circular polarization state. The beam was then focused onto the sample, using a lens with a focal length of 100 mm, and a focal spot size of 80 μm was achieved. That is, placing the sample slightly out-of-focus allowed for adjustment of the spot size at the sample position such that it could cover the entire array. After interaction with the sample, the light was again collimated with a second lens. To facilitate postprocessing, the sample plane was then imaged onto a CCD camera using an additional lens. Measurements were performed on two arrays with L-helices and D-helices for each array period and pitch, 32 measurements in total, to prove the repeatability of sample fabrication and measurement technique. The gray-shadowed areas in Figure 3c,d corresponds to the resulting standard deviation of these measurements.

Supporting Information

Supporting Information is available from the Wiley Online Library or from the author.

Conflict of Interest

The authors declare no conflict of interest.

Author Contributions

G.E. and P.B. contributed equally to this work. V.K. designed and supervised the study. G.E. grew the samples and carried out the measurements with thermal light source. S.R. and N.L. developed the thermal light source experimental setup. P.B., V.S., and M.C. were involved in the measurements with the supercontinuum source. P.B. carried out the numerical simulations. G.E., P.B., and V.K. led the manuscript writeup.

Data Availability Statement

The data that support the findings of this study are available from the corresponding author upon reasonable request.

Code Availability

FDTD simulations were carried out with the commercial software from Ansys Lumerical. Codes are available from the corresponding author upon reasonable request.

[1] A. Lininger, G. Palermo, A. Guglielmelli, G. Nicoletta, M. Goel, M. Hinczewski, G. Strangi, *Adv. Mater.* **2022**, 2107325.

[2] H. Hübener, U. De Giovannini, C. Schäfer, J. Andberger, M. Ruggenthaler, J. Faist, A. Rubio, *Nat. Mater.* **2021**, 20, 438.

[3] D. Ayuso, A. F. Ordonez, P. Decleva, M. Ivanov, O. Smirnova, *Nat. Commun.* **2021**, 12, 3951.

[4] E. S. A. Goerlitzer, A. S. Puri, J. J. Moses, L. V. Poulikakos, N. Vogel, *Adv. Opt. Mater.* **2021**, 9, 2100378.

[5] N. I. Zheludev, Y. S. Kivshar, *Nat. Mater.* **2012**, 11, 917.

[6] Z. Yang, Z. Wang, H. Tao, M. Zhao, *Opt. Express* **2016**, 24, 18266.

[7] N. Yu, F. Capasso, *Nat. Mater.* **2014**, 13, 139.

[8] V. Tasco, M. Esposito, F. Todisco, A. Benedetti, M. Cuscunà, D. Sanvitto, A. Passaseo, *Appl. Phys. A* **2016**, 122, 280.

[9] S. Takahashi, T. Tajiri, Y. Ota, J. Tatebayashi, S. Iwamoto, Y. Arakawa, *Appl. Phys. Lett.* **2014**, 105, 051107.

[10] J. G. Gibbs, A. G. Mark, T. C. Lee, S. Eslami, D. Schamel, P. Fischer, *Nanoscale* **2014**, 6, 9457.

[11] Y. Chen, J. Gao, X. Yang, *Nano Lett.* **2018**, 18, 520.

[12] F. Yang, H. Lin, M. Y. Shalaginov, K. Stoll, S. An, C. Rivero-Baleine, M. Kang, A. Agarwal, K. Richardson, H. Zhang, J. Hu, T. Gu, *Adv. Opt. Mater.* **2022**, 10, 2200721.

[13] A. Martins, K. Li, G. S. Arruda, D. Conteduca, H. Liang, J. Li, B. V. Borges, T. F. Krauss, E. R. Martins, *Adv. Opt. Mater.* **2022**, 10, 2102555.

[14] H. Ren, X. Fang, J. Jang, J. Bürger, J. Rho, S. A. Maier, *Nat. Nanotechnol.* **2020**, 15, 948.

[15] J. Hu, X. Zhao, Y. Lin, A. Zhu, X. Zhu, P. Guo, B. Cao, C. Wang, *Sci. Rep.* **2017**, 7, 41893.

[16] Z. Wang, Y. Wang, G. Adamo, B. H. Teh, Q. Y. S. Wu, J. Teng, H. Sun, *Adv. Opt. Mater.* **2016**, 4, 883.

[17] S. J. Masson, A. Asenjo-Garcia, *Nat. Commun.* **2022**, 13, 2285.

[18] E. Sierra, S. J. Masson, A. Asenjo-Garcia, *Phys. Rev. Res.* **2022**, 4, 023207.

[19] J. M. Caridad, D. McCloskey, J. F. Donegan, V. Krstić, *Appl. Phys. Lett.* **2014**, 105, 233114.

[20] B. Dick, M. J. Brett, T. Smy, *J. Vac. Sci. Technol., B* **2003**, 21, 23.

[21] L. Ohnoutek, B. J. Olohan, R. R. Jones, X. Zheng, H.-H. Jeong, V. K. Valev, *Nanoscale* **2022**, 14, 3888.

[22] J. K. Gansel, M. Thiel, M. S. Rill, M. Decker, K. Bade, V. Saile, G. Von Freymann, S. Linden, M. Wegener, *Science* **2009**, 325, 1513.

[23] J. M. Caridad, D. McCloskey, F. Rossella, V. Bellani, J. F. Donegan, V. Krstić, *ACS Photonics* **2015**, 2, 675.

**ADVANCED
SCIENCE NEWS**

www.advancedsciencenews.com

**ADVANCED
PHOTONICS
RESEARCH**

www.adpr-journal.com

[24] N. Tsutsumi, Y. Takai, K. Kinashi, W. Sakai, *Sci. Rep.* **2021**, *11*, 15860.

[25] J. M. Caridad, C. Tserkezis, J. E. Santos, P. Plochocka, M. Venkatesan, J. M. D. Coey, N. A. Mortensen, G. L. J. A. Rikken, V. Krstić, *Phys. Rev. Lett.* **2021**, *126*, 177401.

[26] K. Höflich, T. Feichtner, E. Hansjürgen, C. Haverkamp, H. Kollmann, C. Lienau, M. Silies, *Optica* **2019**, *6*, 1098.

[27] A. E. Krasnok, A. E. Miroshnichenko, P. A. Belov, Y. S. Kivshar, *Opt. Express* **2012**, *20*, 20599.

[28] Y. Kivshar, A. Miroshnichenko, *Opt. Photonics News* **2017**, *28*, 24.

[29] C. Patzig, B. Rauschenbach, *J. Vac. Sci. Technol., A* **2008**, *26*, 881.

[30] C. Khare, J. W. Gerlach, M. Weise, J. Bauer, T. Höche, B. Rauschenbach, *Phys. Status Solidi A* **2011**, *208*, 851.

[31] C. Khare, J. W. Gerlach, T. Höche, B. Fuhrmann, H. S. Leipner, B. Rauschenbach, *Appl. Surf. Sci.* **2012**, *258*, 9762.

[32] U. Kilic, M. Hilfiker, A. Ruder, R. Feder, E. Schubert, M. Schubert, C. Argyropoulos, *Adv. Funct. Mater.* **2021**, *31*, 2010329.

[33] W. K. Choi, L. Li, H. G. Chew, F. Zheng, *Nanotechnology* **2007**, *18*, 385302.

[34] T. P. McLean, R. Loudon, *J. Phys. Chem. Solids* **1960**, *13*, 1.

[35] Y. Meeda, N. Tsukamoto, Y. Yazawa, Y. Kanemitsu, Y. Masumoto, *Appl. Phys. Lett.* **1991**, *59*, 3168.

[36] G. Gu, M. Burghard, G. T. Kim, G. S. Düsberg, P. W. Chiu, V. Krstić, S. Roth, W. Q. Han, *J. Appl. Phys.* **2001**, *90*, 5747.

[37] Y. Wu, P. Yang, *Chem. Mater.* **2000**, *12*, 605.

[38] G. Milano, M. Aono, L. Boarino, U. Celano, T. Hasegawa, M. Kozicki, S. Majumdar, M. Menghini, E. Miranda, C. Ricciardi, S. Tappertzhofen, K. Terabe, I. Valov, *Adv. Mater.* **2022**, *34*, 2201248.

[39] F. Tu, M. Drost, F. Vollnhals, A. Späth, E. Carrasco, R. H. Fink, H. Marbach, *Nanotechnology* **2016**, *27*, 355302.

[40] M. Masyukov, A. Vozianova, A. Grebenchukov, K. Gubaidullina, A. Zaitsev, M. Khodzitsky, *Sci. Rep.* **2020**, *10*, 3157.

[41] L. A. Ibbotson, A. Demetriadou, S. Croxall, O. Hess, J. J. Baumberg, *Sci. Rep.* **2015**, *5*, 8313.

[42] K. Robbie, M. J. Brett, *J. Vac. Sci. Technol., A* **1997**, *15*, 1460.

[43] M. Esposito, V. Tasco, F. Todisco, A. Benedetti, I. Tarantini, M. Cuscunà, L. Dominici, M. De Giorgi, A. Passaseo, *Nanoscale* **2015**, *7*, 18081.

[44] M. Esposito, M. Manoccio, A. Leo, M. Cuscunà, Y. Sun, E. Ageev, D. Zuev, A. Benedetti, I. Tarantini, A. Passaseo, V. Tasco, *Adv. Funct. Mater.* **2022**, *32*, 2109258.

[45] W. I. L. Lawrie, H. G. J. Eenink, N. W. Hendrickx, J. M. Boter, L. Petit, S. V. Amitonov, M. Lodari, B. Paquelet Wuetz, C. Volk, S. G. J. Philips, G. Droulers, N. Kalhor, F. van Riggelen, D. Brousse, A. Sammak, L. M. K. Vandersypen, G. Scappucci, M. Veldhorst, *Appl. Phys. Lett.* **2020**, *116*, 080501.

[46] S. Connaughton, M. Kolesnik-Gray, R. Hobbs, O. Lotty, J. D. Holmes, V. Krstic, *Beilstein J. Nanotechnol.* **2016**, *7*, 1284.

[47] P. Woźniak, I. De Leon, K. Höflich, C. Haverkamp, S. Christiansen, G. Leuchs, P. Banzer, *Opt. Express* **2018**, *26*, 19275.

[48] Y. Huang, G. Yang, *J. Phys. Chem. C* **2021**, *125*, 812.